JACS
JOURNAL OF THE AMERICAN CHEMICAL SOCIETY
Article
Cite This: J. Am. Chem. Soc. 2019, 141, 7789−7796
pubs.acs.org/JACS

Metal−Organic Framework Nanoparticle-Assisted Cryopreservation of Red Blood Cells

Wei Zhu,[*,†,‡,△] Jimin Guo,[†,△] Jacob Ongudi Agola,[†] Jonas G. Croissant,[†] Zihao Wang,[†] Jin Shang,[§] Eric Coker,[∥] Benyamin Motevalli,[⊥] Andreas Zimpel,[#] Stefan Wuttke,[#,¶] and C. Jeffrey Brinker[*,†]

[†]Center for Micro-Engineered Materials and the Department of Chemical and Biological Engineering, The University of New Mexico, Albuquerque, New Mexico 87131, United States

[§]School of Energy and Environment, City University of Hong Kong, Tat Chee Avenue, Kowloon, Hong Kong SAR, P.R. China

[∥]Applied Optical/Plasma Sciences, Sandia National Laboratories, P.O. Box 5800, MS 1411, Albuquerque, New Mexico 87185-1411, United States

[⊥]Department of Mechanical and Aerospace Engineering, Monash University, Clayton, Victoria 3800, Australia

[#]Department of Chemistry and Center for NanoScience (CeNS), University of Munich (LMU), 81377 Munich, Germany

[¶]School of Chemistry, Joseph Banks Laboratories, University of Lincoln, Lincoln LN6 7TS, United Kingdom

Supporting Information

ABSTRACT: The development of hybrid nanomaterials mimicking antifreeze proteins that can modulate/inhibit the growth of ice crystals for cell/tissue cryopreservation has attracted increasing interests. Herein, we describe the first utilization of zirconium (Zr)-based metal−organic framework (MOF) nanoparticles (NPs) with well-defined surface chemistries for the cryopreservation of red blood cells (RBCs) without the need of any (toxic) organic solvents. Distinguishing features of this cryoprotective approach include the exceptional water stability, low hemolytic activity, and the long periodic arrangement of organic linkers on the surface of MOF NPs, which provide a precise spacing of hydrogen donors to recognize and match the ice crystal planes. Five kinds of Zr-based MOF NPs, with different pore size, surface chemistry, and framework topologies, were used for the cryoprotection of RBCs. A "splat" assay confirmed that MOF NPs not only exhibited ice recrystallization inhibition activities but also acted as a "catalyst" to accelerate the melting of ice crystals. The human RBC cryopreservation tests displayed RBC recoveries of up to ∼40%, which is higher than that obtained via commonly used hydroxyethyl starch polymers. This cryopreservation approach will inspire the design and utilization of MOF-derived nanoarchitectures for the effective cryopreservation of various cell types as well as tissue samples.

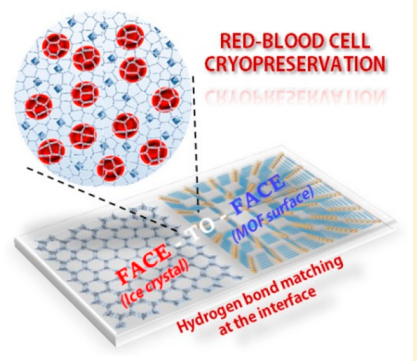

INTRODUCTION

Ice formation and recrystallization are major challenges for cellular cryopreservation.[1,2] The current state-of-the-art strategies for cryopreservation require the addition of high concentrations of cell-permeating cryoprotectants such as water-miscible organic solvents (e.g., dimethyl sulfoxide, glycerol), to minimize ice formation. However, the solvent toxicity and the challenge of removing all traces of toxic solvents prior to transplant or transfusion remains a critical problem for clinical applicability.[3] Natural systems mitigate the deleterious effects of ice formation/recrystallization by producing antifreeze proteins or glycoproteins (AF(G)Ps) that suppress ice formations,[4,5] but extracting natural AF(G)Ps from living organisms is typically an intricate, time-consuming, and expensive process with low yields. Although, currently, many AF(G)Ps can be synthesized or expressed, these proteins are often very expensive and have thermal stability and biocompatibility drawbacks. So far, numerous synthetic compounds and nanomaterials (e.g., hydroxyethyl starch (HES), poly(vinyl alcohol), peptides, oligosaccharides, simple carbohydrates, etc.) that mimic AF(G)Ps have been exploited for cryopreservation applications.[6−8] Gibson and co-workers described the use of synthetic polymers to enhance cell recovery after thawing.[9,10] Matsumura and Hyon demonstrated that polyampholytes have moderate ice recrystallization inhibition (IRI) activities that can be used as cryoprotectants.[11] Ben and co-workers highlighted the use of low-molecular-weight surfactants for inhibiting ice growth.[12] In addition, Wang and co-workers reported the significant IRI activities of nanosized graphene oxide and quasi-carbon nitride quantum dots for cell cryopreservations.[13,14] Nevertheless, the development of new hybrid nanomaterials with potent IRI activities, good biocompatibility/hemocompatibility, and the possibility of easy mass production remains highly desirable.[15,16]

Received: January 30, 2019
Published: April 23, 2019

DOI: 10.1021/jacs.9b00992
J. Am. Chem. Soc. 2019, 141, 7789−7796

Metal−organic frameworks (MOFs) are periodic well-defined porous materials that are typically self-assembled by metal nodes and organic linkers (Scheme 1), offering high control of chemical functionality, pore size, and shape.[17−25] Due to their highly modular nature, MOFs have garnered tremendous interests for many practical applications including gas storage and separation,[26−28] water harvesting,[29,30] chemical catalysis,[31] sensing,[32] energy,[33] drug delivery,[34,35] and biomedical applications.[36−38] Inspired by the well-designed/defined surface coordination chemistry of MOFs, we present a novel strategy for the cryopreservation of red blood cells (RBCs) based on the utilization of water-stable zirconium (Zr)-based MOF nanoparticles (NPs) (Scheme 1). The key point is the negligible hemolytic activity of Zr-based MOF NPs and the periodic arrangement of organic linkers on the MOF outer surface, which provides precise spacing of hydrogen donor groups to recognize and match the prism/basal plane of ice crystals, thus modulating the ice macroscopic activities. Five kinds of Zr-based MOFs including the UiO-66 series of MOFs (UiO-66, UiO-66-NH_2, and UiO-66-OH),[39] UiO-67,[40] and MOF-808,[41] with different pore size, surface chemistry, and framework topology, have been used for cryopreservation demonstration. A dose-dependent assay of all of these MOF NPs displayed low hemolytic activities (<8%) even at a high NP concentrations (5 mg/mL), indicating good hemocompatibility properties. Moreover, a "splat" assay showed that all the MOF NPs exhibited IRI activities. A time-dependent growth assay of the ice crystal formation revealed that the MOF NPs not only inhibit the growth of ice crystals but also may act as a "catalyst" that accelerates the exchange of water molecules at the interface between ice and free water molecules, thereby promoting the melting of ice crystals and consequently increasing the cryopreservation efficiency. In the tests of the cryopreservation of human RBCs, the results show that the UiO-66-OH MOF NPs with the highest density of hydrogen donor groups on the outlayer surface and the best matching to the ice crystal planes exhibited the best cell recovery outcome (~40%), which was higher than that obtained using the commercial polymer (HES) without the addition of any organic solvent, indicating UiO-66-OH MOF NPs to be excellent candidates for cryoprotection. Due to the highly designable nanostructure of MOFs, we believe that our finding will greatly promote the utilization of MOF-inspired nanoarchitectures for cell/tissue cryopreservation applications.

Scheme 1. Description of the Concept Underlying the Synthesis of Metal−Organic Frameworks (Top) and Schematic Illustration of the Utilization of MOF NPs for Cryopreservation of Red Blood Cells Based on Ice Recrystallization Inhibition (Bottom)

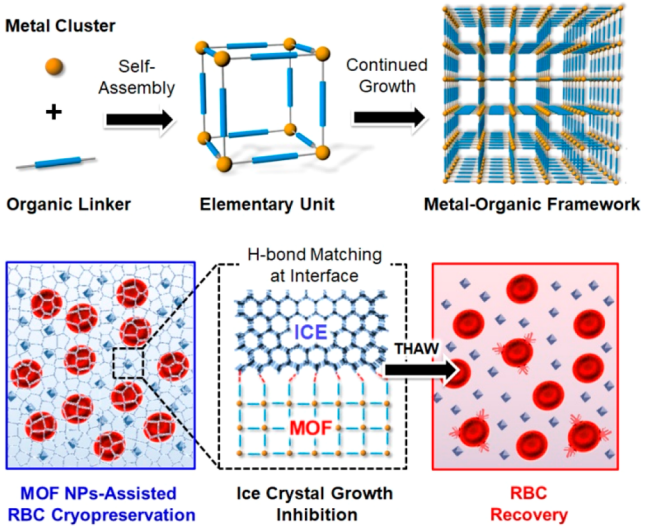

RESULTS AND DISCUSSION

As mentioned, five Zr-based MOF NPs, namely, UiO-66, UiO-66-NH_2, UiO-66-OH, UiO-67, and MOF-808, with different surface chemistries and framework topologies, were selected and synthesized according to the reported solvothermal methods, where the mixed solution containing zirconium salts, the corresponding acid form of organic linkers, and a modulating agent (e.g., formic acid, acetic acid) was heated for a certain time (see materials and methods in the Supporting Information for detailed information). The successful preparation of various MOF NPs was confirmed by a panel of analyses including wide-angle X-ray diffraction (XRD), transmission electron microscopy (TEM), Fourier transform infrared spectroscopy (FTIR), argon (Ar) sorption analyses, and dynamic light scattering.[42] As shown in Figure 1a and Figure S1, XRD analysis confirmed that all of the MOF NPs display crystalline structures matching the corresponding simulations. TEM imaging (Figure S2) reveals the formation of well-defined octahedral shapes for all NPs with uniform sizes of 220, 440, 106, 580, and 678 nm, respectively. FTIR spectroscopy performed on each MOF NP confirmed the presence of the associated enriched functional groups (Figure S3). Moreover, Ar adsorption isotherms (Figure 1b) were all of type I, confirming the permanent microporosity of all the MOF NPs. The related Brunauer−Emmett−Teller surface areas (S_{BET}) were measured to be 1069, 961, 731, 2694, and 1056 m^2/g, respectively (Figure 1c). From single-crystal X-ray analyses, the UiO-66 series of MOFs comprise $Zr_6O_4(OH)_4$ octahedra that are 12-fold connected to the adjacent octahedra through a terephthalic acid linker (BDC) or its derivatives

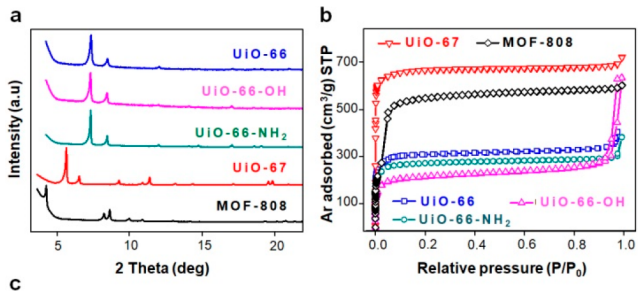

c

MOF	Secondary Building Units	BET surface area (m^2g^{-1})	DFT surface area (m^2g^{-1})	DFT pore diameter (nm)	V_p (mLg^{-1})
UiO-66	$Zr_6O_4(OH)_4(-CO_2)_{12}$	1069	1286	1.2, 2.0	0.52
UiO-66-NH_2	$Zr_6O_4(OH)_4(-CO_2)_{12}$	961	1367	1.6	0.49
UiO-66-OH	$Zr_6O_4(OH)_4(-CO_2)_{12}$	731	855	1.1, 1.5	0.81
UiO-67	$Zr_6O_4(OH)_4(-CO_2)_{12}$	2694	2800	1.5, 2.0	1.12
MOF-808	$Zr_6O_4(OH)_4(-CO_2)_6$	1056	1551	2.2	0.93

Figure 1. Wide-angle powder XRD diffractograms (a) and Ar sorption isotherms (b) of the synthesized MOF NPs: UiO-66, UiO-66-OH, UiO-66-NH_2, UiO-67, and MOF-808. Textural properties of the synthesized MOF NPs (c).

DOI: 10.1021/jacs.9b00992
J. Am. Chem. Soc. 2019, 141, 7789−7796

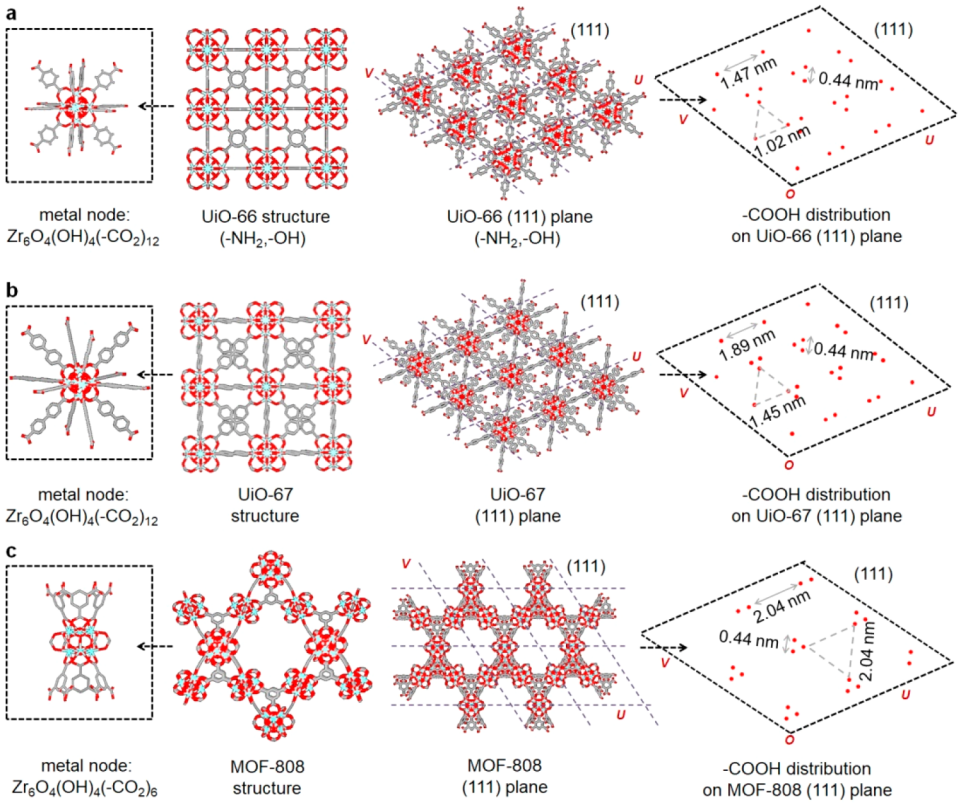

Figure 2. Schematic illustration of the structure features of UiO-66 (−NH_2, −OH) (a), UiO-67 (b), and MOF-808 (c) samples (left to right): metal nodes, crystalline structure, (111) plane, and the related −COOH distribution on the (111) plane.

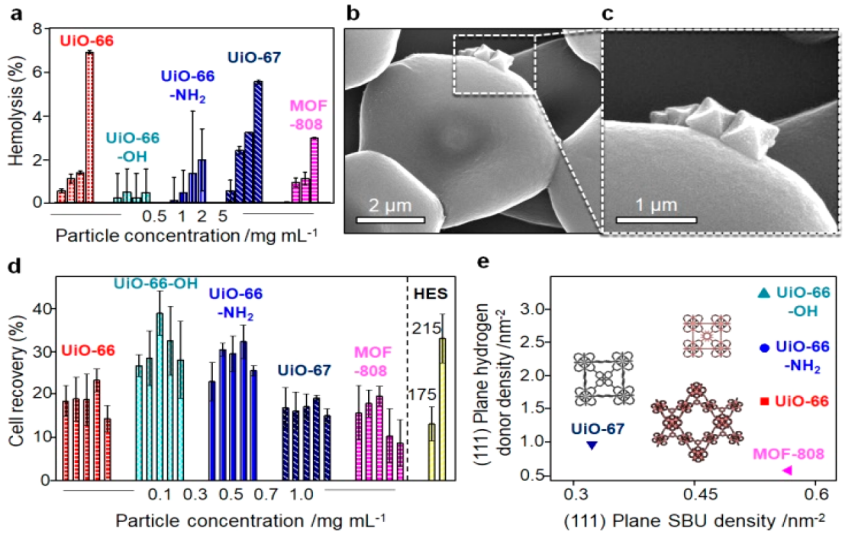

Figure 3. (a) Percent hemolysis of human RBCs upon incubation with MOF NPs with different concentrations. (b,c) SEM images of human RBCs incubated with UiO-66 MOF NPs at room temperature for 3 h. (d) Recovery of human RBCs cryopreserved in MOF NPs or HES polymer (175 or 215 mg mL^{-1}) PBS dispersions with different concentrations and under a stringent test conditions of slow thawing at 4 °C. (e) Image of MOF surface SBU densities on the (111) plane against the density of hydrogen donor groups on the MOF (111) plane.

(BDC-NH_2, BDC-OH),[39] resulting in a structure with fcu topology (Figure 2a). For the isostructural MOF of UiO-67,[40] it shares the same secondary building unit (SBU) of $Zr_6O_4(OH)_4(-CO_2)_{12}$ and fcu topology but with a slightly increased pore size (Figure 2b). For MOF-808,[41] prepared using the tritopic trimesic acid (BTC) as a linker, a different SBU structure of $Zr_6O_4(OH)_4(-CO_2)_6$ was observed, where each SBU is connected to six BTC linkers with each linker coordinated to three SBUs (Figure 2c). MOF-808 has a 6,3-connected three-dimensional (3D) framework with spn topology. Tetrahedral cages possess an internal pore dimension of 4.8 Å, with inorganic SBUs at the vertices and BTC linkers at the face of the tetrahedra. The tetrahedral cages sharing the vertices with each other are further extended in three dimensions to form a stable 3D framework.

DOI: 10.1021/jacs.9b00992
J. Am. Chem. Soc. 2019, 141, 7789−7796

To demonstrate the potential of our synthesized zirconium MOF NPs to enhance RBC cryopreservation, an in vitro blood compatibility experiment was carried out. Before hemolysis testing, the surface zeta-potential for all of the MOF NPs was first measured. As shown in Figure S4, all of the MOF NPs registered a negative charge ranging from −9.4 to −29.1 mV, which should avoid the strong electrostatic interactions between the MOF and RBC surface (zeta-potential = −30 mV)[43] and thus avoid RBC lysis. To examine the hemolytic activity of MOF NPs, different concentrations of MOF NPs were incubated with purified RBCs at 37 °C for 2 h under continuous rotational mixing. DI water (+RBCs) and phosphate-buffered saline (PBS) (+RBCs) were used as the positive control and negative control, respectively. As shown in Figure 3a, the hemolysis percentage increased as the particle concentration increased. Among the five MOF NPs, UiO-66-OH NPs showed the lowest hemolysis percentage (<1%) even at the highest concentration of 5 mg mL^{-1}. Also the highest hemolysis percentage for all MOF NPs was less than 8%, indicating a good overall hemocompatibility. So far, the influence of surface charge, shape, and particle size on the hemolytic activity of RBCs has been reported.[44] In particular, when the NP had a sharp shape, the soft RBC membrane was more easily lysed to cause the fast release of hemoglobin. From TEM images shown in Figure S2, all the MOF NPs showed an octahedral shape with six vertices. To understand the underlying reason for the good hemocompatibility of our synthesized MOF NPs, the interaction between the RBC membrane and UiO-66 MOF NPs that displayed the largest hemolytic activity was assessed. As shown in Figure 3b,c, the UiO-66 MOF NPs are flatly oriented on the surface of the RBCs along their (111) planes with no obvious membrane deformation, which explains the reason for low hemolysis. The low hemolytic activities in all cases highlight the good hemocompability of Zr-based nanoMOFs.

Due to the good hemocompability of MOFs, we envisioned that MOF NPs with well-defined surface chemistries could be excellent candidates for cryopreservation applications. In this study, we chose human red blood cells for cryopreservation studies due to the urgent need to design better strategies of improving RBCs' long-term storage without recourse to any toxic organic solvents.[9,10] Cryopreservation of human RBCs was investigated using a rapid freezing protocol. Briefly, an aqueous suspension of RBC-MOF NPs in 1× PBS solution was rapidly frozen in liquid nitrogen (N_2) and then stored in liquid N_2 for 2 days, followed by a slow thawing process at 4 °C. The thawing at 4 °C was chosen due to the maximum stress it applies to cells, offering a stringent test of the cryopreservative performance of the synthesized MOF NPs.[9,10] As shown in Figure 3d, for all cases tested, the RBC recovery first increased with increasing concentration of MOF NPs and then decreased when the MOF NP concentration reached ca. 1.0 mg mL^{-1}. The highest cell recovery (~40%) occurred for UiO-66-OH MOF NPs at a concentration of 0.5 mg mL^{-1} without any organic solvents. This cell recovery level is better than that achieved by the commercial polymer, HES, at high concentrations of 175 (13.2%) and 215 (32.1%) mg mL^{-1}, highlighting the possibility of using MOFs for cryopreservation applications. Note that from the SEM images in Figure S5, after the cryopreservation process, the RBCs still maintain the original morphologies with biconcave shape, indicating good preservation of the RBC structure. Moreover, the surface SBU densities on the (111) plane versus the density of hydrogen donor groups (−COOH) on the MOF (111) plane was calculated (Figure 3e). Note that for UiO-66-OH and UiO-66-NH_2 MOFs the neighboring hydrogen donor groups (−OH and $-NH_2$) located very close to the carboxylic groups on the top layer surface have also been counted. We observe MOF NPs with higher densities of carboxylic groups (UiO-66-OH and UiO-66-NH_2) on the MOF outer-layer surface to result in a higher cell recovery efficiency. This observation reveals the potential adsorption of MOF NPs onto the ice crystal surface through hydrogen bonding, modulating the growth of ice crystals.

To provide a further understanding of the MOF NP-assisted cryopreservation approach, a "splat" assay commonly used for the quantitative evaluation of the IRI activities was performed. A 10 μL droplet of PBS solution containing various MOF NPs was dropped from a height of approximately 2 m onto a prechilled glass slide (−80 °C) before transfer to a cold stage set at −6 °C under optical microscopy (Figure S6). The mean largest grain size of the ice crystals at different recrystallization times was measured and calculated relative to the negative control (PBS). The smaller the ice crystal size, the higher the IRI activity.[13,14] As shown in Figure 4a,b, compared to the normal PBS solution, the optical microscopy image of the recrystallized ice crystals after the addition of MOF NPs (UiO-66-OH) showed a much smaller ice crystal size, clearly demonstrating the capability of MOF NPs to suppress the recrystallization of ice crystals. Further IRI activity results for various MOFs in PBS dispersions with low particle concentration (0.5 mg mL^{-1}) are shown in Figure 4c. Clearly, all of the MOF NPs exhibited the ability to reduce the grain size of the recrystallized ice crystals. Moreover, as expected, the MOF NPs with a higher density of carboxylic groups on the outer-layer surface of the (111) plane, such as UiO-66-OH and UiO-66-NH_2, showed a higher IRI activity. With an increase of MOF NP concentration to 2 mg mL^{-1} or decrease to 0.1 mg mL^{-1} (Figure 3d), the related IRI activity in each case was

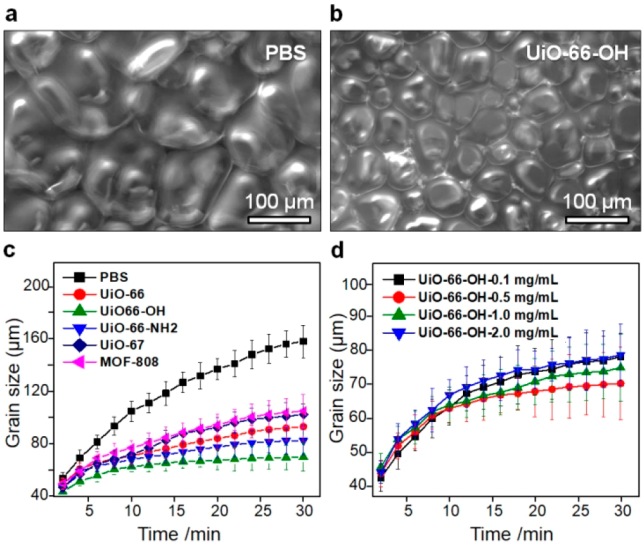

Figure 4. Optical microscopy images of ice crystals grown in PBS solution (a) and in a dispersion of UiO-66-OH MOF NPs in PBS solution (0.5 mg mL^{-1}) (b) after annealing at −6 °C for 30 min. Time-dependent growth of ice crystals in different MOF NPs dispersion solutions (c) and MOF NPs of UiO-66-OH with various concentrations (d).

DOI: 10.1021/jacs.9b00992
J. Am. Chem. Soc. 2019, 141, 7789−7796

weakened to a certain extent. This may be attributed to NP aggregation at high concentrations (Figure S7) causing partial loss of IRI activity or low surface coverage of ice planes by MOF NPs at low concentration causing insufficient ice crystal inhibition. Nevertheless, even at a concentration as low as 0.1 mg mL^{-1}, a potent IRI activity with an arrest of ice crystal growth could still be observed. Furthermore, the impact of MOF NPs on ice formation was also studied by differential scanning calorimetry (DSC). As shown in Figure S8, all of the solutions showed a large exotherm upon cooling (rate = −20 °C min^{-1}) associated with homogeneous ice nucleation at approximately −35 °C compared to approximately −45 °C for PBS. This proves that the presence of MOF NPs in solution enhances the nucleation of ice crystallization, resulting in smaller ice grain size. Furthermore, the crystallinity, that is, the percent of ice crystals in PBS solution, was calculated from the integrated DSC exotherms according to reported equations.[45] Compared to the crystallinity in PBS solution, all of the MOF NP-containing PBS solutions showed lower extents of crystallinity, and the trend was consistent with the densities of carboxylic groups on the MOF outer-layer surface, as shown in Figure 3e. These results demonstrate the ice crystal inhibition activities of Zr-based MOF NPs.

Given that the cryoprotective mechanism involves interactions between the MOF surfaces and associated ice, we expected that the MOF particle size and surface charge would affect the cryoprotective activity. To test this assumption, UiO-66-NH_2 MOF NPs with different sizes (230, 440, and ∼800 nm) (Figures S2 and S9) and surface charges (zeta-potentials = −29.1, −16.6, and −8.9 mV) were synthesized for evaluation of hemolytic activity and RBC recovery. (Please see the detailed information in the Supporting Information for the synthesis and surface modification.) As shown in Figure S10, all three sizes of UiO-66-NH_2 MOF NPs showed low (<3%) and comparable concentration dependencies of percent hemolysis. In tests of the cryopreservation of human RBCs, the results (Figure S11) showed that all the MOF NPs with different sizes exhibited similar levels of RBC recovery, indicating the cell recovery efficacy may be not so sensitive to particle size for MOF NPs that are much smaller than the RBC size. Figure S12 shows the concentration-dependent percent hemolysis for MOFs prepared with different zeta-potentials through modification with phosphocholine chloride calcium salt (PCCS). As the zeta-potential was varied from −29.1 to −16.6 to −8.9 mV, by increasing PCCS modification, the hemolysis percentage of RBC increased. For the NP with the zeta-potential of −8.9 mV, the hemolysis percentage at the particle concentration of 5 mg mL^{-1} can be up to 14.2%, which is much higher than for −29.1 mV (2.2%). This behavior can be attributed to increased interactions between RBCs and MOF NPs. RBC has a highly negatively charged surface. As the MOF NP negative charge is progressively reduced, there is less electrostatic repulsion between the RBCs and MOF NPs, promoting greater RBC/MOF interactions and thus higher RBC hemolysis. Also in the tests of the cryopreservation of RBCs, the results (Figure S13) showed that with the increase of zeta-potential from −29.1 to −8.9 mV, the cell recovery efficacy decreased. For example, when the particle concentration was set to 0.5 mg mL^{-1}, the related cell recovery was found to be decreased from 29.6 to 12.6%. This decrease of cryoprotective activities can be attributed to the introduction of additional coordinated molecules on the MOF surface, which would potentially disrupt the original periodic arrangement of organic linkers, creating in essence surface defects that decrease the hydrogen-bond matching probability between the organic linkers on the MOF surface and water molecules on ice planes. This consequently weakens the IRI activities.

We further analyzed the reason why the investigated MOF NPs exhibited different IRI activities at the molecular level. We hypothesized that the IRI activity could reflect a pattern of hydrogen-bond binding sites on all the MOF outer-layer surfaces stemming from the positions of the respective carboxylic groups of the organic linkers. The carboxylic group distributions on the (111) plane of various MOFs are shown in Figure 2a. Clearly, all of the −COOH distributions display periodic structures and are highly dependent on the original porous crystalline structures. The MOFs of UiO-66, UiO-66-OH, and UiO-66-NH_2 share the same pore structure and have the highest density of −COOH on the (111) plane as their construction incorporates the very short BDC organic linker. The distance between carboxylic groups in two neighboring BDCs in the same SBU or between two close SBUs was measured to be 4.4, 10.2, and 14.7 Å, respectively. For MOF UiO-67, which has the same topology as UiO-66, but with an increase of one organic linker per aromatic ring, the related distance of carboxylic groups changed to 4.4, 14.5, and 18.9 Å, respectively. MOF-808 showed a quite different −COOH group distribution on the (111) plane because of the totally different pore structure. The distance of carboxylic groups was measured as 4.4 and 20.4 Å. In Figure 5a, the basic ice crystal plane of the basal plane, primary prism, and secondary prism is shown. The distance between the hydroxyls on the ice of the basal, primary, and secondary prismatic faces is measured as 4.514, 2.760, and 2.764 Å (Figure S14), respectively.[46] The interval hydroxyls in the primary prismatic face was found to be 7.35 Å.[13,14] Clearly, the carboxylic groups residing in neighboring organic linkers in the same SBU with a separation of 4.4 Å closely match hydroxyl separation distances on the basal plane of ice. On the other hand, neighboring carboxylic groups from the closet SBUs for the UiO-66 series MOF with a separation of 14.7 Å show a perfect fit to the double distance of interval hydroxyls in the primary prismatic face (2 × 7.35 Å). Both fitted distances to the basal plane and primary prism were found in the UiO-66 series MOFs. To determine the preferred ice adsorption plane for various MOFs, the extent of matching of the MOF (111) plane to different ice planes was calculated (Figure S15) based on hydrogen bonding donor/acceptor distances between the MOF (111) surface and ice planes.

The results show that the UiO-66 series of MOF and UiO-67 have a preference to bind to the ice primary plane, and MOF-808 prefers to bind to both the ice primary and secondary prism planes. Due to the additional hydrogen donor groups from the neighboring −OH or −NH_2 groups for UiO-66-OH and UiO-66-NH_2, the increased hydrogen-bond binding sites further enhanced the binding strength between MOF NPs and crystalline ice, thus offering higher IRI activities.

To further understand the distribution of MOF NPs during the ice recrystallization process, UiO-66-NH_2 MOF NPs labeled with green fluorescein isothiocyanate were synthesized, and we conducted a time-dependent ice crystal growth study. As shown in Figure 5b−e and Figure S16, at the very first moment, the fluorescent intensity inside ice crystals is quite strong, indicating the doping of MOF NPs within the ice crystals. With the increase of recrystallization time, the ice

DOI: 10.1021/jacs.9b00992
J. Am. Chem. Soc. 2019, 141, 7789−7796

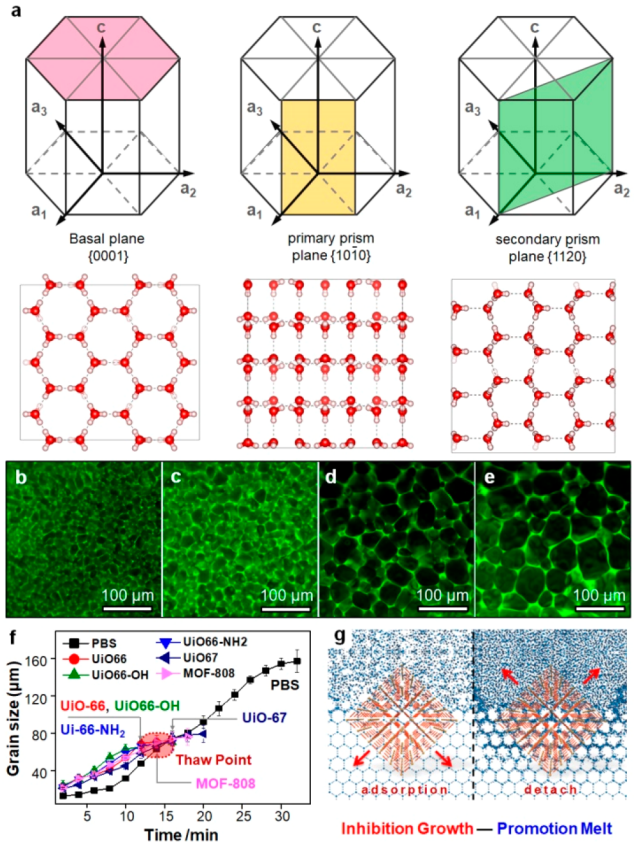

Figure 5. (a) Schematic illustration of the basic ice crystal planes (basal, primary prism, and secondary prism plane) and the related molecular packing of water. The fluorescent image of ice crystal growth in fluorescein isothiocyanate-labeled UiO-66-NH_2 NP dispersions (0.5 mg mL^{-1}) in PBS solutions at different times: 5 s (b), 30 s (c), 4 min (d), and 30 min (e). (f) Time-dependent ice crystal growth in different MOF NP PBS dispersion solutions (0.5 mg mL^{-1}); the annealing process was conducted on a cold stage with a slow increase in temperature from −10 to −2 °C. (g) Schematic illustration of the proposed mechanism of MOF NP ice growth inhibition and melt promotion.

crystals undergo rapid growth in size, where the MOF NPs are expelled from the ice crystals and occupy intervening liquid water gaps. This observation is in conflict with the observed IRI activity in Figure 4c, where MOFs were adsorbed onto the ice surface to inhibit the ice crystal growth. To further reveal the role of MOF NPs during the recrystallization process, the recrystallization of ice crystal on a cold stage with slow temperature increase from −10 to −2 °C was also performed. The rate of increase in stage temperature is shown in Figure S17. As displayed in Figure 5f, the ice crystals from PBS solution without MOF NP addition showed a continuous growth even with the extension of time to 25 min. However, after addition of MOF NPs, a much faster ice crystal melting was observed, where the starting thaw point was at 12 min for UiO-66, UiO-66-NH_2, and UiO-66-OH, 15 min for MOF-808, and 17 min for UiO-67. This phenomenon was again well-correlated with the carboxylic (hydrogen donor) group distribution on the MOF surface in Figure 3e, where the higher density of the hydrogen donor group showed faster ice crystal melting. To explain these results, we noted that compared to the nanosized two-dimensional graphene oxide and quantum dots[13,14] that can easily and strongly adsorb onto the ice crystal plane, the binding strengths between the ice and 3D MOF NPs at the interface are not strong enough to allow MOF NPs to have a stable attachment. During the recrystallization process, the MOF NPs may detach from the ice planes. Due to the interaction between the MOF NPs and the fixed water molecules at the interface, the detachment of MOF NPs may cause the release of fixed water molecules to a "free" state. This attaching and detaching balance makes MOF NPs act as a "catalyst" accelerating the exchange of water molecules at the interface between ice and free water (Figure 5g), thus promoting the melting of the ice crystals and consequently increasing the cryopreservation efficiency due to shorter exposure to ice crystals. Both ice growth inhibition and melting promotion make MOF NPs excellent candidates as a cryoprotectants.

In summary, by mimicking the antifreeze proteins in inhibiting ice growth/recrystallization and protecting living cells from freezing damage, for the first time we have shown that Zr-based MOF NPs can be used for cell cryopreservation applications. Our investigations also show that Zr-based nanoMOFs not only show potent IRI activities against ice growth/recrystallization but also act as a "catalyst" to accelerate the exchange of water molecules at the interface between ice and free liquid water. Through the cryopreservation of human RBCs, we have demonstrated that the nanosized UiO-66-OH MOF NP is a promising new kind of cryoprotectant. The unique capability of MOFs to inhibit ice crystal growth possibly benefiting from the hydrogen-bond matching at the interface between ice crystal planes and MOF outer-layer surfaces with long and precise periodic arrangement will greatly promote the design and synthesis of new MOF-inspired nanoarchitectures for cryopreservation and bioapplications.

■ ASSOCIATED CONTENT

Supporting Information

The Supporting Information is available free of charge on the ACS Publications website at DOI: 10.1021/jacs.9b00992.

Supplementary experiments and structure characterization data (PDF)

■ AUTHOR INFORMATION

Corresponding Authors

*zhuw200461170@163.com

*jbrinker@unm.edu

ORCID

Jin Shang: 0000-0001-5165-0466

C. Jeffrey Brinker: 0000-0002-7145-9324

Present Address

‡School of Biology and Biological Engineering, South China University of Technology, 382 East Outer Loop Road, University Park, Guangzhou 510006, P.R. China.

Author Contributions

△W.Z. and J.G. contributed equally.

Notes

The authors declare no competing financial interest.

■ ACKNOWLEDGMENTS

C.J.B. acknowledges support by the Sandia National Laboratory Laboratory-Directed Research and Development Program and support from the Department of Energy Office of

DOI: 10.1021/jacs.9b00992
J. Am. Chem. Soc. 2019, 141, 7789−7796

Science, Division of Materials Science and Engineering. Sandia National Laboratories is a multimission laboratory managed and operated by National Technology and Engineering Solutions of Sandia, LLC, a wholly owned subsidiary of Honey-well International, Inc., for the U.S. Department of Energy's National Nuclear Security Administration under Contract No. DENA-0003525. W.Z. and J.G. acknowledge help from Tianrun Zhang for setting up the cryostage.

REFERENCES

(1) Biggs, C. I.; Bailey, Tl L.; Graham, B.; Stubbs, C.; Fayter, A.; Gibson, M. I. Polymer mimics of biomacromolecular antifreezes. *Nat. Commun.* **2017**, *8*, 1546.
(2) He, Z.; Liu, K.; Wang, J. Bioinspired Materials for Controlling Ice Nucleation, Growth, and Recrystallization. *Acc. Chem. Res.* **2018**, *51* (5), 1082−1091.
(3) Asghar, W.; El Assal, R.; Shafiee, H.; Anchan, R. M.; Demirci, U. Preserving human cells for regenerative, reproductive, and transfusion medicine. *Biotechnol. J.* **2014**, *9* (7), 895−903.
(4) Liu, K.; Wang, C.; Ma, J.; Shi, G.; Yao, X.; Fang, H.; Song, Y.; Wang, J. Janus effect of antifreeze proteins on ice nucleation. *Proc. Natl. Acad. Sci. U. S. A.* **2016**, *113* (51), 14739−14744.
(5) Liou, Y.-C.; Tocilj, A.; Davies, P. L.; Jia, Z. Mimicry of ice structure by surface hydroxyls and water of a β-helix antifreeze protein. *Nature* **2000**, *406*, 322−324.
(6) Deller, R. C.; Pessin, J. E.; Vatish, M.; Mitchell, D. A.; Gibson, M. I. Enhanced non-vitreous cryopreservation of immortalized and primary cells by ice-growth inhibiting polymers. *Biomater. Sci.* **2016**, *4*, 1079−1084.
(7) Drori, R.; Li, C.; Hu, C.; Raiteri, P.; Rohl, A. L.; Ward, M. D.; Kahr, B. A. A Supramolecular Ice Growth Inhibitor. *J. Am. Chem. Soc.* **2016**, *138* (40), 13396.
(8) Capicciotti, C. J.; Kurach, J. D. R.; Turner, T. R.; Mancini, R. S.; Acker, J. P.; Ben, R. N. Small molecule ice recrystallization inhibitors enable freezing of human red blood cells with reduced glycerol concentrations. *Sci. Rep.* **2015**, *5*, 9692.
(9) Deller, R. C.; Vatish, M.; Mitchell, D. A.; Gibson, M. I. Synthetic polymers enable non-vitreous cellular cryopreservation by reducing ice crystal growth during thawing. *Nat. Commun.* **2014**, *5*, 3244.
(10) Mitchell, D. E.; Lovett, J. R.; Armes, S. P.; Gibson, M. I. Combining Biomimetic Block Copolymer Worms with an Ice-Inhibiting Polymer for the Solvent-Free Cryopreservation of Red Blood Cells. *Angew. Chem., Int. Ed.* **2016**, *55* (8), 2801−2804.
(11) Matsumura, K.; Hyon, S. H. Polyampholytes as low toxic efficient cryoprotective agents with antifreeze protein properties. *Biomaterials* **2009**, *30* (27), 4842−4849.
(12) Capicciotti, C. J.; Leclere, M.; Perras, F. A.; Bryce, D. L.; Paulin, H.; Harden, J.; Liu, Y.; Ben, R. N. Potent inhibition of ice recrystallization by low molecular weight carbohydrate-based surfactants and hydrogelators. *Chem. Sci.* **2012**, *3*, 1408−1416.
(13) Geng, H.; Liu, X.; Shi, G.; Bai, G.; Ma, J.; Chen, J.; Wu, Z.; Song, Y.; Fang, H.; Wang, J. Graphene Oxide Restricts Growth and Recrystallization of Ice Crystals. *Angew. Chem., Int. Ed.* **2017**, *56* (4), 997−1001.
(14) Bai, G.; Song, Z.; Geng, H.; Gao, D.; Liu, K.; Wu, S.; Rao, W.; Guo, L.; Wang, J. Oxidized Quasi-Carbon Nitride Quantum Dots Inhibit Ice Growth. *Adv. Mater.* **2017**, *29* (28), 1606843.
(15) Bhowmick, D.; Srivastava, S.; D'Silva, P.; Mugesh, G. Highly Efficient Glutathione Peroxidase and Peroxiredoxin Mimetics Protect Mammalian Cells against Oxidative Damage. *Angew. Chem., Int. Ed.* **2015**, *54* (29), 8449−8453.
(16) Li, W.; Liu, Z.; Liu, C.; Guan, Y.; Ren, J.; Qu, X. Manganese Dioxide Nanozymes as Responsive Cytoprotective Shells for Individual Living Cell Encapsulation. *Angew. Chem., Int. Ed.* **2017**, *56* (44), 13661−13665.
(17) Furukawa, H.; Cordova, K. E.; O'Keeffe, M.; Yaghi, O. M. The chemistry and applications of metal-organic frameworks. *Science* **2013**, *341* (6149), 1230444.
(18) Bétard, A.; Fischer, R. A. Metal−organic framework thin films: from fundamentals to applications. *Chem. Rev.* **2012**, *112* (2), 1055−1083.
(19) Cohen, S. M. Postsynthetic methods for the functionalization of metal−organic frameworks. *Chem. Rev.* **2012**, *112* (2), 970−1000.
(20) Stock, N.; Biswas, S. Synthesis of metal-organic frameworks (MOFs): routes to various MOF topologies, morphologies, and composites. *Chem. Rev.* **2012**, *112* (2), 933−969.
(21) Murray, L. J.; Dincă, M.; Long, J. R. Hydrogen storage in metal−organic frameworks. *Chem. Soc. Rev.* **2009**, *38*, 1294−1314.
(22) Li, J.; Sculley, J.; Zhou, H. Metal−organic frameworks for separations. *Chem. Rev.* **2012**, *112* (2), 869−932.
(23) Ma, L.; Abney, C.; Lin, W. Enantioselective catalysis with homochiral metal−organic frameworks. *Chem. Soc. Rev.* **2009**, *38*, 1248−1256.
(24) Farha, O. K.; Hupp, J. T. Rational design, synthesis, purification, and activation of metal− organic framework materials. *Acc. Chem. Res.* **2010**, *43* (8), 1166−1175.
(25) Moghadam, P. Z.; Li, A.; Wiggin, S. B.; Tao, A.; Maloney, A. G. P.; Wood, P. A.; Ward, S. C.; Fairen-Jimenez, D. Development of a Cambridge Structural Database subset: a collection of metalramework materials. d composites. s for Individual. *Chem. Mater.* **2017**, *29* (7), 2618−2625.
(26) McDonald, T. M.; Mason, J. A.; Kong, X.; Bloch, E. D.; Gygi, D.; Dani, A.; Crocellà, V.; Giordanino, F.; Odoh, S. O.; Drisdell, W. S.; Vlaisavljevich, B.; Dzubak, A. L.; Poloni, R.; Schnell, S. K.; Planas, N.; Lee, K.; Pascal, T.; Wan, L. F.; Prendergast, D.; Neaton, J. B.; Smit, B.; Kortright, J. B.; Gagliardi, L.; Bordiga, S.; Reimer, J. A.; Long, J. R. Cooperative insertion of CO_2 in diamine-appended metal-organic frameworks. *Nature* **2015**, *519*, 303−308.
(27) Bobbitt, N. S.; Mendonca, M. L.; Howarth, A. J.; Islamoglu, T.; Hupp, J. T.; Farha, O. K.; Snurr, R. Q. Metal−organic frameworks for the removal of toxic industrial chemicals and chemical warfare agents. *Chem. Soc. Rev.* **2017**, *46*, 3357−3385.
(28) Adil, K.; Belmabkhout, Y.; Pillai, R. S.; Cadiau, A.; Bhatt, P. M.; Assen, A. H.; Maurin, G.; Eddaoudi, M. Gas/vapour separation using ultra-microporous metal−organic frameworks: insights into the structure/separation relationship. *Chem. Soc. Rev.* **2017**, *46*, 3402−3430.
(29) Kim, H.; Yang, S.; Rao, S. R.; Narayanan, S.; Kapustin, E. A.; Furukawa, H.; Umans, A. S.; Yaghi, O. M.; Wang, E. N. Water harvesting from air with metal-organic frameworks powered by natural sunlight. *Science* **2017**, *356* (6336), 430−434.
(30) Kalmutzki, M.; Diercks, C. S.; Yaghi, O. M. Metal−Organic Frameworks for Water Harvesting from Air. *Adv. Mater.* **2018**, *30* (37), 1704304.
(31) Rogge, S. M. J.; Bavykina, A.; Hajek, J.; Garcia, H.; Olivos-Suarez, A. I.; Sepúlveda-Escribano, A.; Vimont, A.; Clet, G.; Bazin, P.; Kapteijn, F.; Daturi, M.; Ramos-Fernandez, E. V.; Llabrés i Xamena, F. X.; Van Speybroeck, V.; Gascon, J. Metal−organic and covalent organic frameworks as single-site catalysts. *Chem. Soc. Rev.* **2017**, *46*, 3134−3184.
(32) Stassen, I.; Burtch, N.; Talin, A.; Falcaro, P.; Allendorf, M.; Ameloot, R. An updated roadmap for the integration of metal−organic frameworks with electronic devices and chemical sensors. *Chem. Soc. Rev.* **2017**, *46*, 3185−3241.
(33) Hendon, C. H.; Rieth, A. J.; Korzyński, M. D.; Dincă, M. Grand Challenges and Future Opportunities for Metal−Organic Frameworks. *ACS Cent. Sci.* **2017**, *3* (6), 554−563.
(34) Lismont, M.; Dreesen, L.; Wuttke, S. Metal-Organic Framework Nanoparticles in Photodynamic Therapy: Current Status and Perspectives. *Adv. Funct. Mater.* **2017**, *27* (14), 1606314.
(35) Zhu, W.; Xiang, G.; Shang, J.; Guo, J.; Motevalli, B.; Durfee, P.; Agola, J. O.; Coker, E. N.; Brinker, C. J. Versatile Surface Functionalization of Metal−Organic Frameworks through Direct Metal Coordination with a Phenolic Lipid Enables Diverse Applications. *Adv. Funct. Mater.* **2018**, *28* (16), 1705274.

DOI: 10.1021/jacs.9b00992
J. Am. Chem. Soc. 2019, 141, 7789−7796

(36) Freund, R.; Lächelt, U.; Gruber, T.; Rühle, B.; Wuttke, S. Multifunctional efficiency: extending the concept of atom economy to functional nanomaterials. *ACS Nano* **2018**, *12* (3), 2094−2105.
(37) Alsaiari, S. K.; Patil, S.; Alyami, M.; Alamoudi, K. O.; Aleisa, F. A.; Merzaban, J. S.; Li, M.; Khashab, N. M. Endosomal Escape and Delivery of CRISPR/Cas9 Genome Editing Machinery Enabled by Nanoscale Zeolitic Imidazolate Framework. *J. Am. Chem. Soc.* **2018**, *140* (1), 143−146.
(38) Doonan, C.; Riccò, R.; Liang, K.; Bradshaw, D.; Falcaro, P. Metal−organic frameworks at the biointerface: synthetic strategies and applications. *Acc. Chem. Res.* **2017**, *50* (6), 1423−1432.
(39) Cavka, J. H.; Jakobsen, S.; Olsbye, U.; Guillou, N.; Lamberti, C.; Bordiga, S.; Lillerud, K. P. A new zirconium inorganic building brick forming metal organic frameworks with exceptional stability. *J. Am. Chem. Soc.* **2008**, *130* (42), 13850−13851.
(40) DeCoste, J. B.; Peterson, G. W.; Jasuja, H.; Glover, T. G.; Huang, Y.; Walton, K. S. Stability and degradation mechanisms of metal−organic frameworks containing the $Zr_6O_4(OH)_4$ secondary building unit. *J. Mater. Chem. A* **2013**, *1*, 5642−5650.
(41) Furukawa, H.; Gándara, F.; Zhang, Y.; Jiang, J.; Queen, W. L.; Hudson, M. R.; Yaghi, O. M. Water adsorption in porous metal−organic frameworks and related materials. *J. Am. Chem. Soc.* **2014**, *136* (11), 4369−4381.
(42) Hirschle, P.; Preiβ, T.; Auras, F.; Pick, A.; Völkner, J.; Valdepérez, D.; Witte, G.; Parak, W. J.; Rädler, J. O.; Wuttke, S. Exploration of MOF nanoparticle sizes using various physical characterization methods−is what you measure what you get? *CrystEngComm* **2016**, *18*, 4359−4368.
(43) Bondar, O. V.; Saifullina, D. V.; Shakhmaeva, I. I.; Mavlyutova, I. I.; Abdullin, T. I. Monitoring of the zeta potential of human cells upon reduction in their viability and interaction with polymers. *Acta Naturae* **2012**, *4*, 78−81.
(44) Abbaraju, P. L.; Meka, A. K.; Song, H.; Yang, Y.; Jambhrunkar, M.; Zhang, J.; Xu, C.; Yu, M.; Yu, C. Asymmetric Silica Nanoparticles with Tunable Head−Tail Structures Enhance Hemocompatibility and Maturation of Immune Cells. *J. Am. Chem. Soc.* **2017**, *139* (18), 6321−6328.
(45) Liang, J.; Huang, Y.; Zhang, L.; Wang, Y.; Ma, Y.; Guo, T.; Chen, Y. Molecular-Level Dispersion of Graphene into Poly(vinyl alcohol) and Effective Reinforcement of their Nanocomposites. *Adv. Funct. Mater.* **2009**, *19* (14), 2297−2302.
(46) Weng, L.; Stott, S. L.; Toner, M. Molecular dynamics at the interface between ice and poly (vinyl alcohol) and ice recrystallization inhibition. *Langmuir* **2018**, *34* (17), 5116−5123.

DOI: 10.1021/jacs.9b00992
J. Am. Chem. Soc. 2019, 141, 7789−7796